In situ readout of DNA barcodes and single base edits facilitated by in vitro transcription

Amjad Askary[1], Luis Sanchez-Guardado[1], James M. Linton[1], Duncan M. Chadly[1], Mark W. Budde[1], Long Cai [1], Carlos Lois[1] and Michael B. Elowitz [1,2]*

Molecular barcoding technologies that uniquely identify single cells are hampered by limitations in barcode measurement. Readout by sequencing does not preserve the spatial organization of cells in tissues, whereas imaging methods preserve spatial structure but are less sensitive to barcode sequence. Here we introduce a system for image-based readout of short (20-base-pair) DNA barcodes. In this system, called Zombie, phage RNA polymerases transcribe engineered barcodes in fixed cells. The resulting RNA is subsequently detected by fluorescent in situ hybridization. Using competing match and mismatch probes, Zombie can accurately discriminate single-nucleotide differences in the barcodes. This method allows in situ readout of dense combinatorial barcode libraries and single-base mutations produced by CRISPR base editors without requiring barcode expression in live cells. Zombie functions across diverse contexts, including cell culture, chick embryos and adult mouse brain tissue. The ability to sensitively read out compact and diverse DNA barcodes by imaging will facilitate a broad range of barcoding and genomic recording strategies.

Molecular recording systems could revolutionize the study of development and disease by allowing reconstruction of dynamic, single-cell developmental histories from endpoint measurements[1]. In these systems, individual cells actively record information within their genome by continuous editing of uniquely identifiable engineered genomic target sites, or barcodes[2–9]. Multiple methods that use CRISPR–Cas9 or site-specific recombinases to produce barcode diversity have now been developed[2–4,10–13]. One of the most promising approaches is the use of CRISPR base editors, in which a catalytically impaired Cas9 is fused to deaminases and other enzymes to target mutations to specific nucleotides without generating double-stranded breaks[8,9].

In these approaches, readout of barcode edits is most often done by sequencing, which is sensitive to single-nucleotide variations and can be performed at high throughput. However, sequencing-based approaches disrupt spatial organization of cells within tissues, and often recover information only from a minority of cells[14]. The ability to accurately and efficiently read out single-cell barcode edits in situ would link dynamic developmental history with spatial multicellular organization, which is essential for the function of many biological systems.

Recent work has produced an explosion of methods for in situ detection of nucleic acids. These include strategies for combinatorially encoding a large diversity of transcripts[15–18], techniques for amplifying signal from single mRNA molecules[19–23] and approaches for in situ sequencing[24–28]. These methods could be used to detect barcodes transcribed in living cells before fixation. However, ensuring detectable barcode expression across a diverse population of living cells can be challenging owing to stochastic silencing, bursty expression and unintended cell-type-dependent promoter activity. Eliminating the need for expression in living cells could therefore simplify the design of barcode systems. In addition, some methods only detect large-scale differences in target sequence and therefore cannot access single-nucleotide variations. For example, a recent demonstration of recording was based on detection of large-scale

barcode deletions[2]. Thus, a simple and effective strategy for discriminating barcode edits in fixed tissues has been lacking.

Here we introduce an in situ detection method that is sensitive to single-nucleotide edits and can be applied in diverse organismal contexts. It uses well-characterized RNA polymerases from the bacteriophages T3, T7 and SP6 to transcribe genomically integrated barcodes in fixed cells, producing an amplified RNA product that can then be detected using single-molecule FISH (smFISH)[19] or hybridization chain reaction (HCR)[21,29]. Phage polymerases are known to be efficient and specific for their target promoters[30], but have not, to our knowledge, been previously applied in fixed cells. Because it is based on 'waking up' otherwise transcriptionally 'dead' (silent) barcodes in fixed cells, we term the technique Zombie, for 'Zombie is optical measurement of barcodes by in situ expression'. We showed that Zombie efficiently detects short (20-base-pair (bp)) barcodes, accurately discriminates single-nucleotide variants (SNVs) and detects edits made by base editors, without requiring endogenous expression. These capabilities allow for compact virally delivered combinatorial barcode libraries, and set the stage for future recording applications. Furthermore, the simplicity and robustness of this system enables it to function not only in cell culture but also in chick embryos and adult mouse brain tissues.

Results

Phage RNA polymerases can transcribe synthetic DNA barcodes in fixed cells. We first set out to develop a method for specifically amplifying and detecting barcodes integrated in the genome (Fig. 1a). We designed a construct, labeled Z1 (Fig. 1b), containing a previously described 900-bp barcode sequence[2] downstream of tandem SP6, T7 and T3 phage promoters, along with a histone 2B (H2B)–cerulean fluorescent protein (CFP) fusion under the control of the constitutive mammalian CAG promoter for imaging of cell nuclei. We integrated Z1 site specifically at the ROSA26 locus in mouse embryonic stem (mES) cells. We also made a similar cell line with a control construct that lacks the phage promoters (Fig. 1b).

[1]Division of Biology and Biological Engineering, California Institute of Technology, Pasadena, CA, USA. [2]Howard Hughes Medical Institute and Department of Applied Physics, California Institute of Technology, Pasadena, CA, USA. *e-mail: melowitz@caltech.edu
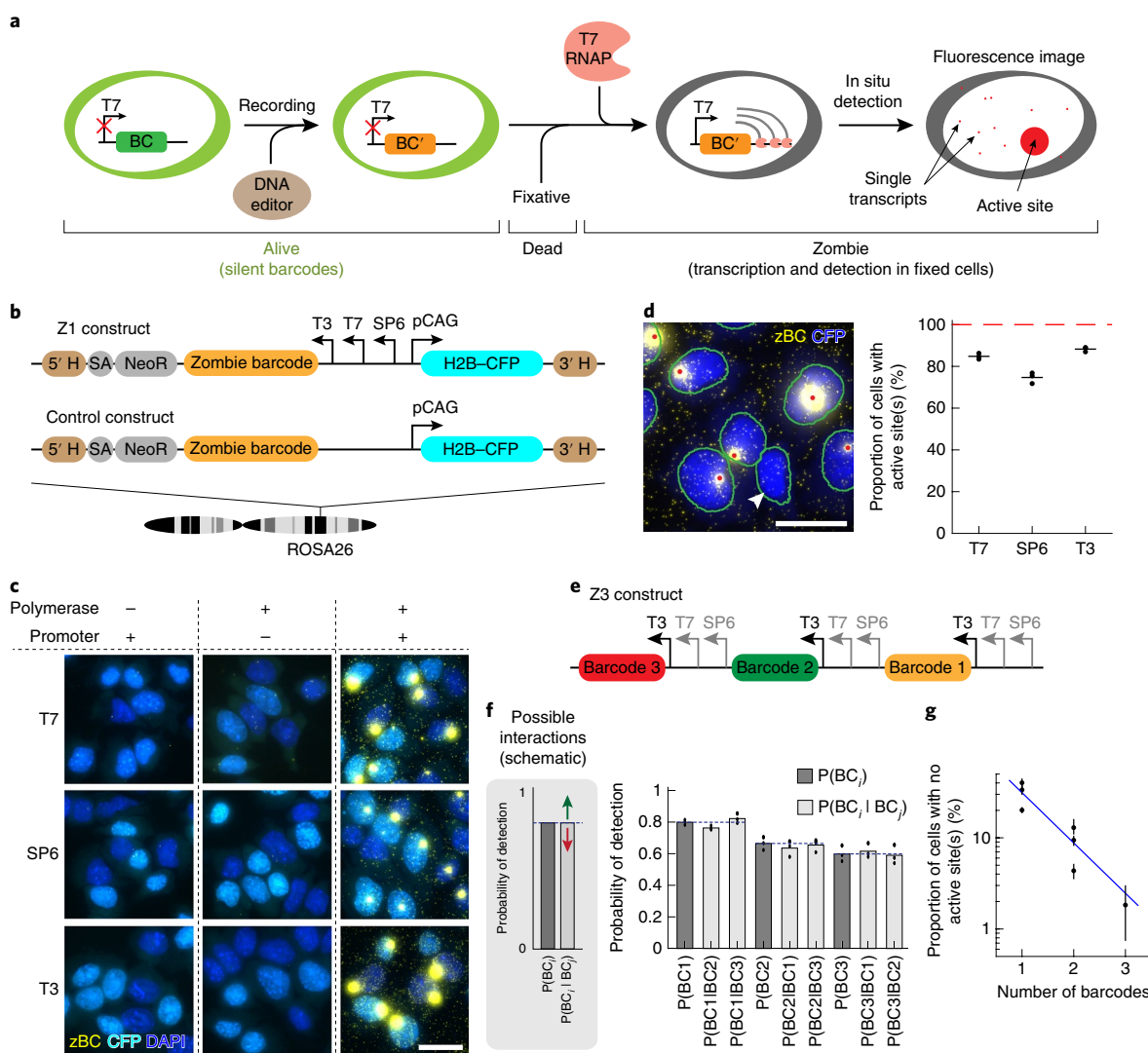
Fig. 1 | Phage RNA polymerases enable in situ readout of DNA barcodes without in vivo expression. a, Workflow for analysis of Zombie barcodes (left to right). First, barcode constructs containing a phage promoter that is inactive in live cells, such as T7, are integrated in the genome. Second, and optionally, base editors or other DNA-modifying enzymes (brown) can alter barcode sequence to increase barcode diversity. Third, cells are fixed and phage RNA polymerase (RNAP; pink) is added. This enables transcription of the barcode to RNA (gray lines). RNA transcripts accumulate at the active site (large red dot) and also diffuse away from it (small red dots represent individual transcripts). **b**, The Z1 construct was engineered to contain a barcode downstream of T3, T7 and SP6 phage promoters, and to express H2B–CFP in living cells from a divergently oriented mammalian promoter. Z1 was stably integrated in mES cells at the ROSA26 locus (single integration per genome). This line was compared to a similar cell line containing the control construct lacking phage promoters. **c**, Polyclonal control cells and Z1 cells (columns) were imaged with or without the indicated phage polymerases (rows). HCR was used to detect barcode RNA (zBC). Nuclei are visualized by native fluorescence of H2B–CFP (cyan) as well as DAPI staining (blue). Barcode transcripts appear only in Z1 cells with phage polymerase (yellow dots, right column). The experiment was independently repeated twice with similar results. Scale bar, 25 μm. **d**, In monoclonal cultures, active sites can be detected in most cells (image). Nuclei (blue) and active sites (yellow) are segmented automatically (green outlines and red dots, respectively). One cell in this field of view does not show any active site (arrowhead). Scale bar, 25 μm. Percentages of cells with detectable active sites for each polymerase are shown on the right. Horizontal lines indicate the mean of replicates ($n = 3$ biologically independent samples). In total, 3,916 cells were analyzed, with at least 420 cells for each replicate. **e**, The Z3 construct encodes three 900-bp barcodes, each expressed from a distinct set of phage promoters. This construct was integrated at ROSA26, transcribed using T3 RNA polymerase, and imaged in all three color channels. T7 and SP6 promoters are shaded gray because they are not used in **f** and **g**. Sizes of elements are not drawn to scale. **f**, Schematic: assuming independence, the conditional probability of detecting barcode i in a cell, given detection of another barcode j, should equal the overall probability of barcode i detection, with deviations signifying either synergy (green arrow) or interference (red arrow) between barcodes. Bar plot: for Z3, the conditional probability analysis shows independent detection events for all three barcodes. Bars indicate the mean of three replicates (points). **g**, The fraction of Z3 cells with no detectable active sites declines with the number of barcodes analyzed, consistent with independent expression of different phage promoters in the same cell. Thus, detection efficiency can be increased with additional barcode copies. Dots represent the mean for different barcodes or barcode combinations and black vertical lines show the range over three replicates. Blue line indicates the exponential fit. Total of 564 cells were analyzed for plots in **f** and **g**.

To detect the barcode, we grew polyclonal populations of cells, fixed them, added each of the phage RNA polymerases and performed HCR with a set of split initiator probes[21] to detect RNA

transcripts (Methods). Fluorescence imaging revealed two types of dots: bright fluorescent dots within cell nuclei and more numerous, but considerably dimmer, diffraction-limited dots scattered

throughout the nucleus and cytoplasm (Fig. 1c). Neither type of dot was observed when either the phage promoters or polymerase were omitted (Fig. 1c). Parental cells lacking a barcode exhibited no dots when cultured alone, but showed some overlapping dimmer dots when co-cultured with engineered cells (Supplementary Fig. 1). These results suggest that the bright dots reflect phage-polymerase-dependent transcription at the integration site, whereas the dimmer dots reflect individual transcripts that can diffuse away from the cell in which they were produced. Together, this barcode design and analysis protocol enable in situ expression and detection of genomically integrated barcodes at integration sites.

We next sought to quantify the efficiency of detection. We selected a monoclonal line with exactly one integration per diploid genome, termed mES-Z1. Within the clone, we consistently detected one or two bright dots in the majority of cells, likely owing to variations in cell cycle phase at the time of fixing, with a small fraction of cells missing any bright dots (Fig. 1d and Supplementary Fig. 2). While we were able to detect the transcription active sites efficiently with all three phage RNA polymerases, the average detection efficiencies of T3 (88%) and T7 (85%) were higher than that of SP6 (75%) (Fig. 1d). Variations in efficiencies may reflect the relative positions of the promoters in the construct, relative amounts of active enzymes, as well as intrinsic differences between the polymerases.

A lack of barcode detection could result if certain cells are impermeable to polymerases or otherwise do not permit in situ transcription. Alternatively, it could reflect intrinsic stochasticity in the polymerization reaction. To distinguish these possibilities, we engineered a second line containing a single integration of a construct termed Z3, in which three barcodes are each controlled by a separate set of phage promoters and can be detected using distinct fluorescence channels (Fig. 1e). If non-detection is a property of the individual cells, we would expect to predominantly detect either all three barcodes or no barcodes (strong correlation). By contrast, in a stochastic transcription model, we would expect that detection of one barcode would not affect the probability of detecting another barcode (weak correlation).

Analysis of active site co-localization in 564 cells revealed no significant correlation or pairwise mutual information between any pair of barcodes (χ^2 test, P values of 0.7970, 0.1917 and 0.1256 for the three pairs; Supplementary Fig. 3). The chance of detecting each barcode in a cell was independent of detection of the other barcodes (Fig. 1f). Consistent with this observation, the fraction of cells with no detected active sites declined exponentially with the number of barcodes analyzed in the same cell at the rate expected from the single-barcode detection frequencies (Fig. 1g). Together, these data suggest that detection is a stochastic event that occurs independently at each barcode. Therefore, although a fraction of barcodes fail to produce detectable signal, the false-negative rate per cell can be reduced by increasing the barcode copy number. This property may be valuable in the study of rare cell types, where capturing information from a majority of cells is essential.

Zombie enables reliable in situ detection of 20-bp DNA barcodes. Barcode transcription produces multiple RNA molecules from the same template in close proximity, which effectively amplifies the barcode target and could facilitate robust detection of short barcodes. To test this, we hybridized fixed mES-Z1 cells after the in vitro transcription step with three orthogonal 20-bp probes targeting regions downstream of the phage promoters (Fig. 2a). We then analyzed the binding of these probes, by both smFISH and HCR[29,31]. In both analyses, we observed easily detectable transcription active sites in all three channels (Fig. 2b and Supplementary Fig. 4). For all three phage RNA polymerases, the active sites could be detected in a large fraction of cells (Fig. 2c), and most dots were redundantly detected in multiple channels (Fig. 2d). These results show that barcodes as short as 20 bp can be efficiently and reliably detected in situ.

Zombie enables in situ detection of single-nucleotide mismatches. Discrimination of small sequence differences could facilitate imaging-based barcoding applications. While structured and toehold probes can be used to detect single-nucleotide variations by leveraging base pairing within the probe[32–36], traditional probes can bind to target sequences even when they contain a single-nucleotide mismatch[32] (Supplementary Fig. 5). We hypothesized that simultaneously competing multiple probes, each containing a distinct nucleotide at a single site, for binding to the many transcripts present in an active site could lead to preferential binding of exact match probes over mismatch probes, and thereby enable nucleotide identification (Fig. 3a).

To test this idea, we fixed mES-Z1 cells, performed in vitro transcription with T7 RNA polymerase and targeted a 20-bp region of the Z1 barcode with four probes, each containing a distinct nucleotide at a single position, and each detectable with orthogonal HCR initiators in different fluorescence channels (Fig. 3b). To control for systematic differences among fluorescent dyes, we performed each analysis with four different fluorescence channel permutations (Fig. 3c and Supplementary Fig. 6) and quantified the relative fluorescence intensities of each channel for each active site. We performed this analysis four times, once for each possible nucleotide at the variable position (Fig. 3c,d and Supplementary Fig. 6).

When targeting A, C or G, we observed a strong preference for the correct target nucleotide (Fig. 3d) across different color–HCR initiator permutations, ranging between 92% and 96% for A, 79% and 93% for C and 93% and 99% for G (percentages indicate the fraction of fluorescent dots that are 'called' correctly by the algorithm). Some inaccurate calls may be explained by non-specific background HCR amplification in a region that overlaps with the cell nuclei but is not a true active site. However, when targeting U, in addition to the matched A probes, detectable signal was also observed from the mismatched G probes (Supplementary Fig. 6), which is consistent with wobble base pairing between U and G[37]. Nevertheless, the base calling algorithm detected the correct match probe in three out of four permutations tested, with 90%, 97% and 85% accuracy (Fig. 3d).

To investigate the dependence of SNV discrimination on the position of the variant nucleotide within the probe, we performed a similar analysis with SNVs in positions 1 through 7 of the probes (Supplementary Fig. 7). Positions 2 through 7 provided accurate SNV discrimination. Furthermore, this analysis provided additional examples of accurate discrimination when U is the target (Supplementary Fig. 7). These results indicate that probe competition can enable accurate in situ identification of SNVs.

Zombie reads out in vivo barcode base edits. CRISPR base editors have recently emerged as powerful tools for precise and predictable genome editing[38–42]. They can target and edit genomic DNA with single-base-pair resolution in a multiplexable manner. Heritable somatic mutations created by base editors could enable subsequent reconstruction of cell lineage and event histories[1,8,9]. The ability to read out base edits by imaging, rather than sequencing, would enable lineage and event history recording approaches that preserve spatial information, operate in individual cells and could allow accurate recovery of sequence information from a high fraction of cells[2]. As Zombie allows in situ detection of single-nucleotide mismatches, we next asked whether it could be combined with base editors to read out changes in single base pairs in a synthetic memory unit.

We engineered 31-bp barcodes that could be edited by the adenine base editor (ABE)[40] and a corresponding guide RNA (gRNA; Fig. 4a). We concatenated these barcodes into ~500-bp arrays, preceded by phage promoters. Using lentiviral vectors, we incorporated multiple array copies into the genome of HEK293T cells to create the Z-MEM cell lines (Fig. 4a). We then transiently
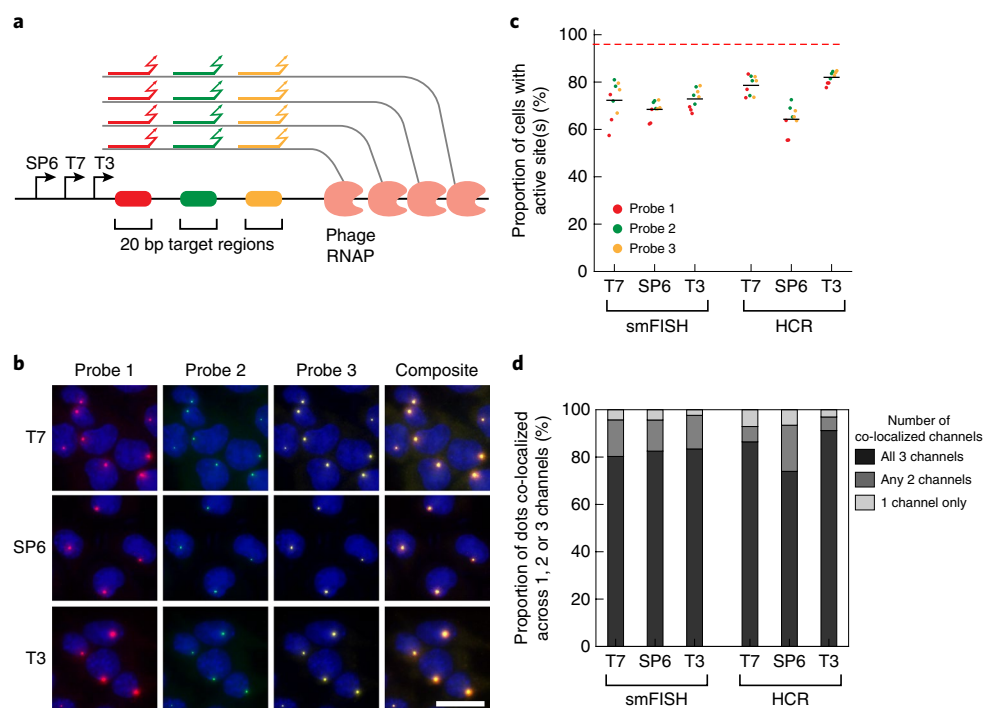
Fig. 2 | Reliable detection of short barcodes. a, Short probes (colored lines) target 20-bp regions of the larger Z1 barcode sequence and can be detected in distinct fluorescence channels. Local accumulation of transcripts at the active site effectively amplifies signal and enables detection, even with a single probe per target site. **b**, Z1 cells were treated with each polymerase (rows) and imaged in three channels (columns) after detection with individual fluorescently labeled probes (colors matching those in **a**). The final column shows composite images. The barcode in Z1 cells is integrated site specifically at the ROSA26 locus. The experiment was independently repeated three times with similar results. Scale bar, 25 μm. **c**, Signal from each individual probe can be detected in the majority of the cells by smFISH or HCR. Plot shows the percentage of Z1 cells with active sites detected using a single 20-bp probe. Dots are color-coded on the basis of probe identity. Data are from three biologically independent samples. Lines show the average efficiency over three probes and three replicates. **d**, Co-localization analysis shows that the majority of dots co-localize in multiple channels, indicating the reliability of single-probe detection. For each condition, gray shades indicate the fraction of dots that are detected in only one channel or co-detected in two or three channels. Data from three biologically independent samples are combined in each condition. For plots in **c** and **d**, a total of 5,097 cells were analyzed, with at least 669 cells for each condition.

co-transfected plasmids expressing the ABE (ABE7.10)[40], the gRNA and a fluorescent co-transfection marker (for example, green fluorescent protein (GFP)) into Z-MEM cells, and cultured cells for 5 d. To analyze editing, we fixed cells, added T3 RNA polymerase and detected transcribed barcodes using competing probes with distinct HCR initiators for edited and unedited states. This analysis was performed pairwise, on adjacent barcodes. As a negative control, we also performed the analysis on cells that did not receive ABE or gRNA.

We designed two types of synthetic memory arrays (Fig. 4b). Design 1 enables independent addressing of different barcodes by distinct gRNAs, facilitating multichannel recording. By contrast, design 2 uses one gRNA to edit all 12 barcodes, allowing a single gRNA to generate greater sequence diversity. In both cases, editing should result in changes in single base pairs in corresponding barcodes.

In both designs, individual barcodes showed an approximately binary response in imaging, appearing in either the edited or unedited channel, but not both (Fig. 4c). Moreover, pairwise analysis of the adjacent barcodes verified independent addressing in design 1 and multiplexed addressing in design 2 (Fig. 4d). We next quantified the signal intensity for each dot, in the edited and unedited channels, with or without co-transfection of ABE and gRNA (Fig. 4e and Supplementary Figs. 8–10). Without ABE or gRNA most dots clustered in a single region (Fig. 4e). By contrast, when ABE and gRNA were both present a second cluster appeared, with a larger mean ratio of edited to unedited probe intensity (Fig. 4e), reflecting successful editing in a substantial fraction of cells (Fig. 4f).

We observed similar behavior with the other analyzed barcodes (Supplementary Figs. 9 and 10). We then used k-means clustering to classify the active sites as edited or unedited, with bootstrap resampling allowing determination of confidence for each assignment (Supplementary Figs. 8–10). In both designs, except for a small subpopulation (Supplementary Figs. 9 and 10), active sites could be robustly classified on the basis of their relative signal intensity.

A key parameter for recording is the edit rate, defined as the probability of an edit occurring at a given unedited target site per unit time. To estimate the relative edit rates of different barcodes, we tabulated the percentage of dots that were edited for each barcode in each design (Fig. 4f). These values varied widely across ten distinct design 1 barcodes, from 1.6% to 19.7% with a median of 12.9% (probes for the two remaining units failed to generate signal and were not considered in the analysis). A broad range of edit rates, such as that observed here, has been shown to be advantageous in recording applications[43]. Similarly, design 2 units were edited at rates ranging from 15.5% to 51.5% with a median 31.3%. By contrast, memory units that were not targeted showed apparent edit rates close to 0 (Fig. 4f), consistent with both strong targeting specificity by ABE and accurate amplification and readout by Zombie. In a separate experiment, we showed that the edit rates measured by Zombie are similar to those measured by next-generation sequencing for the same set of barcodes, further validating the accuracy of Zombie in situ readout (Supplementary Fig. 11). Together, these results show that base editing can be targeted to distinct memory units and read out quantitatively in situ with high fidelity by Zombie.
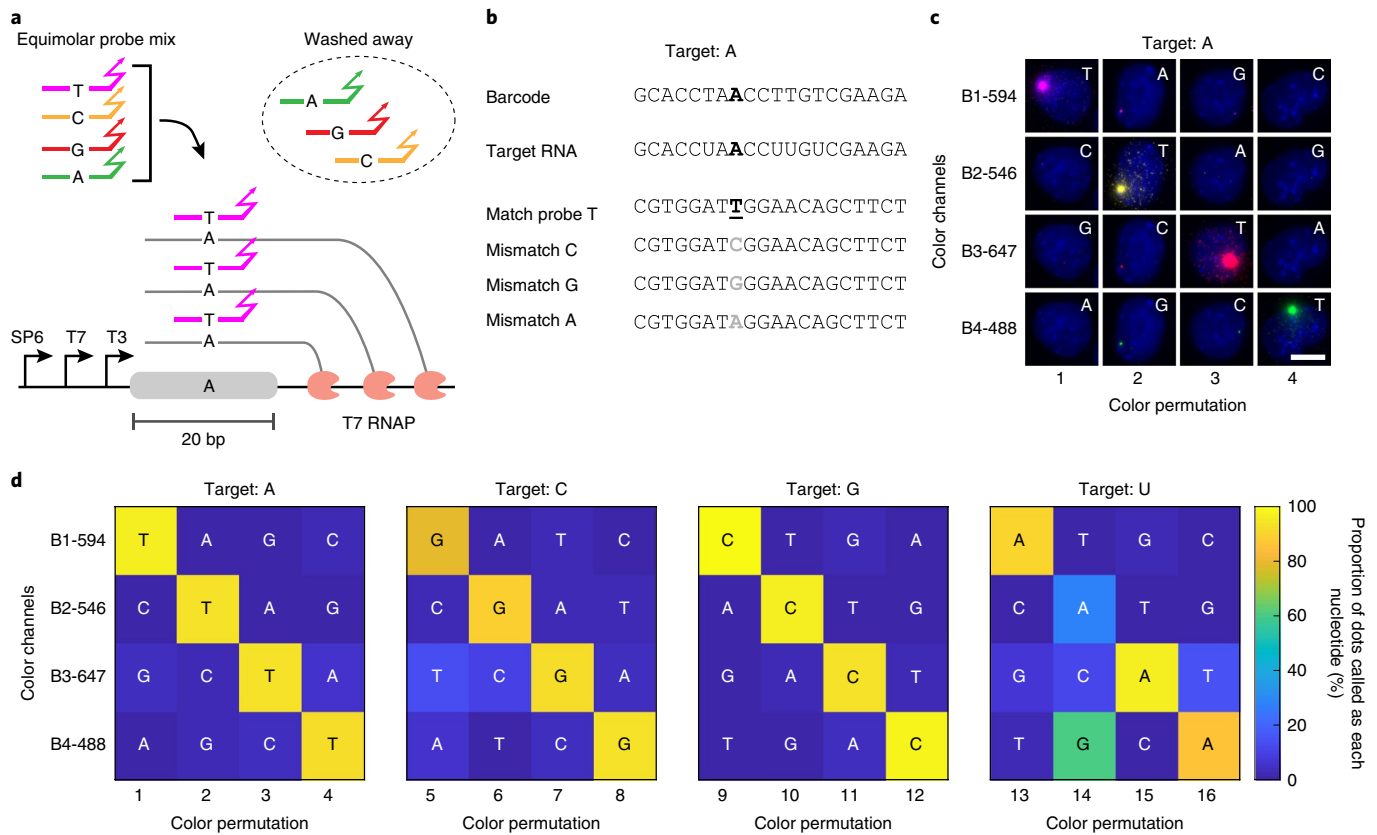
Fig. 3 | Probe competition accurately discriminates SNVs. a, Perfect match probes outcompete those with a single mismatch when an equimolar mixture of all four probe variants is used. This feature can be used to detect SNVs in situ. **b**, Sequences of barcode, target RNA and probes with SNV position indicated in bold underline (match) and gray (mismatch). **c**, Representative images of Z1 cells showing detection of the correct target nucleotide in the barcode (see **d** for quantification of the results and Supplementary Fig. 6 for representative images of other target nucleotides). All images were acquired under the same conditions and displayed with identical processing parameters for each channel (row). Each column represents one experiment in which four probes with an SNV and orthogonal HCR initiators (B1–B4) were mixed and hybridized to the sample with the indicated color permutation. Letters indicate the probe variant in each image. The HCR initiator and the fluorescence channel used for each probe are shown next to the rows. The barcode in Z1 cells is integrated site specifically in ROSA26 locus. Scale bar, 10 μm. **d**, Probe competition can detect all four target nucleotides. Each matrix represents SNV analysis with four distinct color permutations, as in **c**, with the indicated target nucleotide at distinct positions. For targeting U (right-most matrix), one permutation (14) is ambiguous owing to wobble base pairing, but others (for example, 15) provide accurate discrimination. The color scale represents the percentage of dots in which the indicated color channel has the highest rank of normalized brightness (Methods). A total of 4,009 cells were analyzed, with at least 135 cells for each color permutation.

Zombie identifies compact barcodes in embryonic and adult tissues. Reconstructing lineage information in embryos, brains and tumors requires the ability to discriminate among a set of distinct barcodes or barcode edits in complex spatially organized contexts[2–7,13]. To test Zombie readout within tissues, we engineered a lentivirus, termed ZL1, containing probe target sequences downstream of phage promoters, along with a divergently oriented, constitutively expressed fluorescent protein reporter to enable identification of transduced cells (Fig. 5a). We first injected the lentivirus into the lumen of the developing chick neural tube at stage HH10 (ref. [44]), and analyzed embryos 3 d later at stage HH27 (Fig. 5a). In a parallel study, we analyzed Zombie readout in adult mouse brain tissues, focusing on the olfactory bulb, which incorporates newly generated neurons in the adult stage[45]. We injected the ZL1 lentivirus into the granular cell layer of the olfactory bulb and killed the mice for analysis 3 d later (Fig. 5a). In both cases, we observed robust, T7 polymerase-dependent in situ barcode transcription within the transduced regions (Fig. 5b). Together, these results show that Zombie can be used to detect viral barcodes in embryonic and adult tissue.

We next tested the ability to discriminate single-base-pair mismatches in the same chick and mouse contexts. We analyzed tissues with an equimolar mixture of perfect-match and single-base-mismatch probes, along with a third reference probe targeting a distinct downstream region, each in a distinct color channel (Fig. 5c). As a control, we also swapped color channels for the match and mismatch probes. Match probes strongly outcompeted mismatch probes, regardless of the color channel, in both organisms (Fig. 5d,e). Further, matching probes co-localized with reference probes, indicating that match–mismatch probe competition does not hinder detection efficiency (Fig. 5d,e). Taken together, these results demonstrate that Zombie can discriminate between single-base-pair mismatches in chick embryos and adult mouse brains.

Many in vivo barcoding and recording applications require simultaneous analysis of multiple barcode variants. To assess this capability, we designed three pairs of distinctly barcoded lentiviruses. Each virus contained two distinct 20-bp barcodes, each containing an A or a G at a designated variable position. Critically, we designed these viruses such that the identity of the variable base in one barcode matched that of the other barcode in the same virus (Fig. 5f). With this design, two barcodes on the same virus should appear strongly correlated in the variable base, while barcodes on different viruses should vary independently. We selected A and G to mimic possible outcomes of base editing (Fig. 4a).
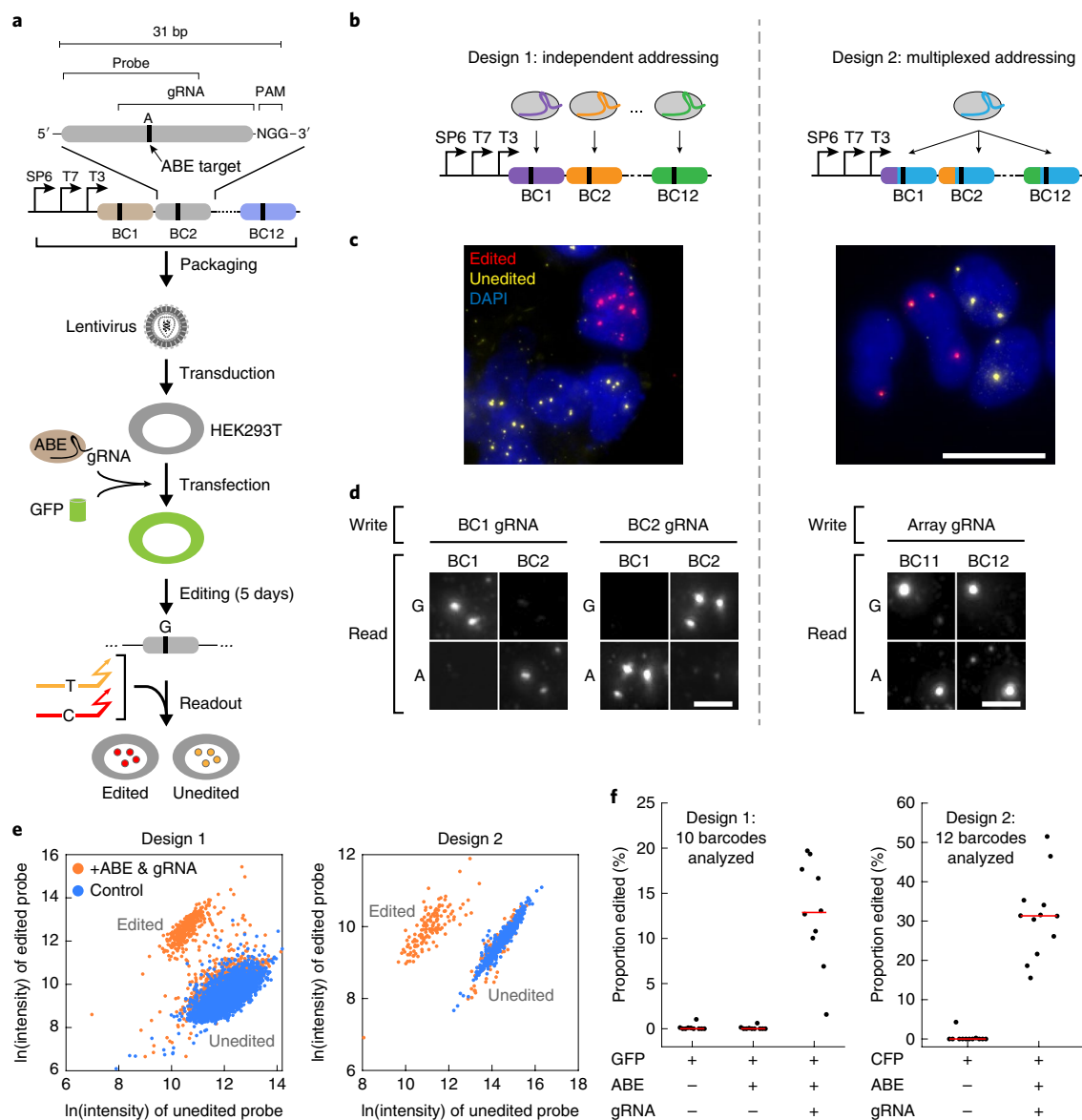
Fig. 4 | CRISPR base edits can be read out in situ. a, Arrays of 12 barcodes were designed so that, in each barcode, a single base pair (black vertical line) can be targeted by the ABE and a gRNA. The barcode arrays were packaged in lentivirus and transduced into HEK293T cells. ABE7.10, gRNA and a fluorescent co-transfection marker (for example, GFP), were transiently delivered as DNA into the cells, and editing was allowed to occur for 5 d. Finally, cells were fixed, treated with T3 RNA polymerase and read out by competing probes for original (orange) and edited (red) base variants. **b**, Two designs of the memory array. Design 1 allows each barcode to be edited independently by a distinct gRNA, whereas all barcodes in design 2 are targeted by the same gRNA, providing more memory states for an individual gRNA. In both designs, the state of each individual barcode can be read out in situ using Zombie. **c**, Representative images, for design 1 (left) and design 2 (right), showing a mixture of edited (red) and unedited (yellow) active sites. As barcodes are delivered by lentiviral transduction, cells can carry multiple copies of the barcode in their genome. The experiment was independently repeated twice with similar results. Scale bar, 10 μm. **d**, Each barcode in design 1 (left) can be addressed independently using its corresponding gRNA. Matrices (2 × 2) show results of targeting distinct barcodes. Edits are seen at the targeted barcode but not the adjacent non-targeted barcode. By contrast, design 2 gRNA (right) can edit all barcodes. The experiment was independently repeated twice with similar results. Scale bar, 3 μm. **e**, Analysis of barcode 1, design 1 (left) and barcode 10, design 2 (right). Dots can be classified into distinct edited and unedited groups on the basis of the signal intensity in edited and unedited channels. Scatter plots show the natural log of the intensity in edited versus unedited channels. Data from negative control samples (blue) are plotted on top of points from samples which received both ABE7.10 and gRNA plasmids. See Supplementary Figs. 9 and 10 for all barcodes in both designs. **f**, Edits are detected when both ABE and gRNA are present. Each point represents one barcode, red lines show the median. Without ABE and barcode-specific gRNA, only a very small fraction of active sites are misidentified as edited, indicating low false-positive rates across barcodes. Note that editing rates differ among barcodes (vertical scatter). On average 1,357 and 383 active sites were analyzed for each barcode at each condition, for designs 1 and 2, respectively.

We simultaneously injected mouse olfactory bulbs with a mixture of these three viral pairs. Twelve days later, we used Zombie with three consecutive rounds of hybridization and imaging to read out all pairs of viral barcodes. Single-nucleotide differences between barcodes were readily identifiable on the basis of the relative signal intensity of competing probes (Fig. 5g and Supplementary Fig. 12). Furthermore, as expected, we observed a strong correlation between the state of two barcodes appearing on the same virus, at each Zombie active site (Fig. 5g,h). Overall, 92% of sites were classified correctly as either A or G for both barcodes (Fig. 5h). Some of the
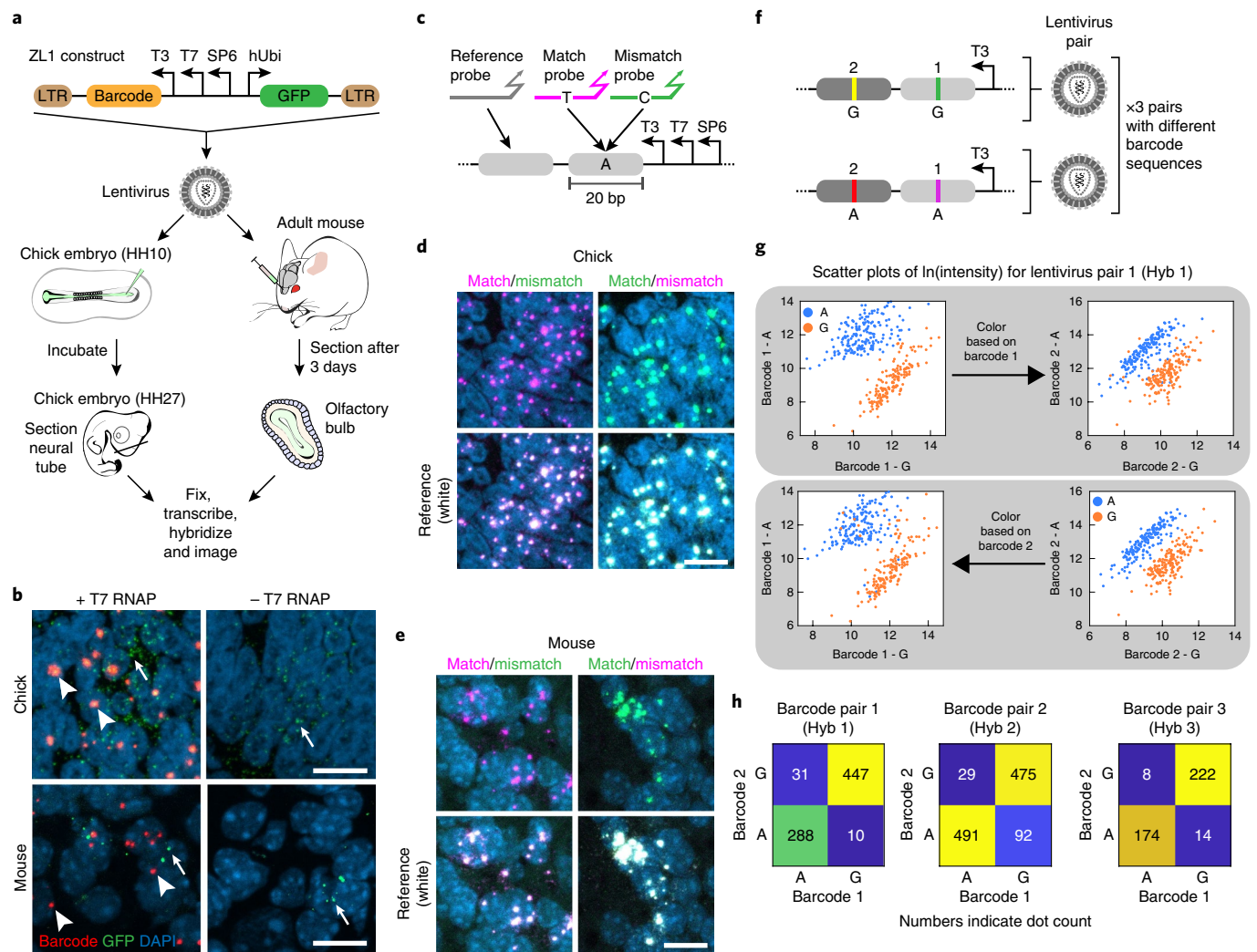
Fig. 5 | Zombie can detect barcodes and discriminate SNVs in chick embryo and adult mouse brain. a, The ZL1 construct includes a barcode downstream of phage promoters, a human ubiquitin C promoter (hUbi) controlling GFP expression to allow identification of transduced cells and long terminal repeat (LTR) sequences to facilitate lentiviral delivery. ZL1 was packaged in lentivirus and injected into the olfactory bulb of a 3-month-old mouse or chick neural tube at embryonic stage HH10. Chick embryos were incubated for 3 d after transduction, until stage HH27, and then frozen and sectioned for analysis of the neural tube. Mouse brains were frozen and sectioned 3 d after transduction to analyze olfactory bulb. Both samples were then fixed, treated with T7 RNA polymerase, probed and imaged. **b**, In coronal sections through the diencephalon of chick embryos, we observed distinct active sites (arrowheads) with, but not without, transcription by T7 RNA polymerase. Similarly, Zombie active sites could also be detected, in a T7-dependent manner, in the granular cell layer of the olfactory bulb (arrowheads). Although the expression of GFP, detected by HCR, was sparse (arrows), the injection site could still be identified. All experiments were repeated on at least three sections with similar results. **c**, To test for detection of single-base-pair mismatches in mouse and chicken tissue sections, samples were hybridized with match and mismatch probes (pink and green, respectively). A reference probe independently identified the active sites. **d,e**, In both chicken (**d**) and mouse (**e**) samples, fluorescent signal at active sites was dominated by the match probe, regardless of channel assignments (columns). Match probes also co-localized with reference channels (bottom rows), indicating that competition between match and mismatch probes does not reduce overall detection efficiency. All experiments were repeated on at least three sections with similar results. As barcodes are delivered by lentiviral injection, cells can carry multiple copies of the barcode in their genome. Scale bars, 10 μm. **f**, Pairs of barcoded lentiviral vectors were used to further assess the SNV detection capability in vivo. Each virus contains two distinct 20-bp barcodes, denoted by 1 and 2. Within a pair, viruses have variants of these barcodes that differ from each other at only one base pair (A or G). A mix of three viral pairs, with different barcode sequences but the same SNV arrangement, was simultaneously injected into the mouse olfactory bulb and read out in three rounds of hybridization and imaging 12 d after transduction. **g**, Scatter plots showing the natural log of signal intensity for two variants (A and G) of two barcodes (1 and 2) for lentivirus pair 1 (see Supplementary Fig. 12 for the other pairs). Each point represents one active site. The points are color coded on the basis of their barcode 1 state (top) or barcode 2 state (bottom) to show the concordance between the detected state of two barcodes. **h**, In all pairs, the majority of active sites are classified as either A or G for both barcodes. Data are combined from two biological replicates.

remaining sites, classified as A for one barcode and G for another, might be explained by integration of both members of a lentivirus pair at sites too close to be spatially resolved (Supplementary Fig. 13). Together, these results indicate that Zombie permits multiplexed barcode readout with single-base discrimination in brain tissue.

Combinatorial barcode libraries (Fig. 6a) could provide an exponentially increasing number of distinct barcodes with only a linear increase in the number of hybridization and imaging cycles needed to read them out[46]. The ability to detect short (20-bp) DNA barcodes in situ should facilitate construction and delivery of such
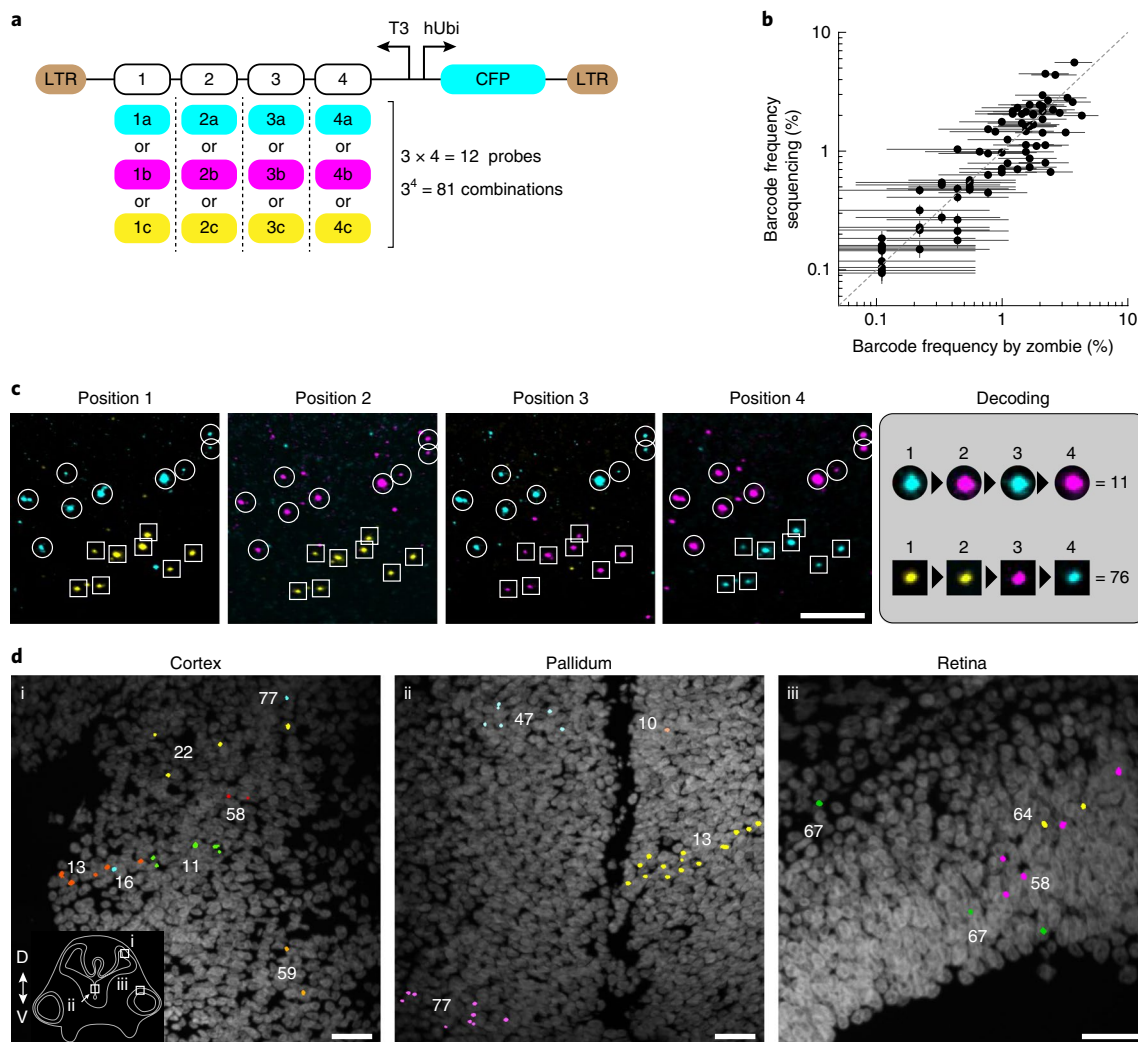
Fig. 6 | In situ readout of a combinatorial barcode library. a, A combinatorial lentiviral library in which each of four positions can take one of three distinct position-specific 20-bp barcodes to generate 81 possible barcode combinations. The viruses also encode CFP downstream of a human ubiquitin promoter. **b**, The frequency at which barcode combinations are detected in situ, in transduced HEK293T cells, is consistent with the frequency measured by next-generation sequencing. Each point represents one barcode combination. A total of 906 active sites were analyzed by Zombie. Error bars are 95% binomial confidence intervals, calculated using the Clopper–Pearson method. As the number of observations by imaging (906 active sites) is lower than the sequencing read count (102,056 aligned reads), the horizontal error bars are wider than the vertical ones. **c**, Detection of two clones of cells, labeled by two barcode combinations, in a coronal section of chick neural tube. Maximum-intensity-projected images corresponding to variants in each barcode position are merged in three color channels (cyan, magenta and yellow, corresponding to **a**). Dots that do not appear consistently in all rounds are excluded from the analysis. **d**, Examples of cells in developing chick cortex (i), pallidum (ii), and retina (iii) labeled with various barcode combinations (arbitrary colors). The inset shows the approximate location of the panels on a drawing of a coronal section through chick neural tube and indicates dorsal (D) and ventral (V) directions. For **c** and **d**, two embryos were analyzed. Thirty-nine of 81 barcode combinations were identified in one embryo by analyzing 44 images acquired from ten sections. In the other embryo, we identified 20 distinct barcode combinations in 11 images acquired from six consecutive sections. In **d**, distinct barcode combinations are labeled in arbitrary colors, that is, there is no relation to the colors in **c**. Scale bars, 25 μm.

libraries. As a proof of principle, we constructed a lentiviral library containing 81 distinct combinations of 12 barcode sequences, each 20 bp long (Fig. 6a). We transduced HEK293T cells with this library and read out the library in three rounds of hybridization and imaging, each one probing four of 12 barcodes with orthogonal color channels (Supplementary Fig. 14). In this analysis, barcode combinations were detected at frequencies consistent with those measured by next-generation sequencing (Fig. 6b), corroborating the accuracy of in situ readout.

In a parallel in vivo study, we injected the combinatorial library into the lumen of the developing neural tube of stage HH11 chick embryos. Three days later (stage HH27), we froze the embryos, performed the Zombie procedure, and analyzed in three rounds

of hybridization, as with the HEK293T cells (Fig. 6c). We detected cells with distinct combinations of barcodes in both neural tube and retina of chick embryos (Fig. 6d). In many instances, cells labeled with the same barcode combination were observed close to each other and organized in a way that suggests clonal relationship (Fig. 6d; clone 13). In other cases, despite relatively sparse labeling, cells with different barcode combinations were intermixed, indicating the necessity for high barcode diversity in establishing clonal relationships (Fig. 6d; clones 13, 16 and 11). These results demonstrate how Zombie can facilitate the use of combinatorial barcode libraries with imaging readout both in vitro and in vivo.

Finally, an ideal barcode readout system would be compatible with analysis of endogenous gene expression. To test this, we

analyzed gene expression alongside barcode detection in the olfactory bulb of mice injected with the paired viruses (Fig. 5f). Using HCR, we confirmed that *Tbx21* (expressed by projection neurons) and Tyrosine hydroxylase (*Th*; expressed by periglomerular cells) could be detected alongside barcodes, in the mitral and glomerular layers, respectively, as expected[47,48](Supplementary Fig. 15). This analysis demonstrates the suitability of Zombie for barcoding and recording applications that require readout of endogenous gene expression as well as barcodes in tissue samples.

Discussion

Here we showed that phage RNA polymerases enable imaging-based barcode readout in individual fixed cells, producing easily detectable fluorescent dots localized to transcriptional sites (Fig. 1). Transcription enabled detection of 20-bp barcodes (Fig. 2) with discrimination of SNVs using competing probes (Fig. 3). This capability further enabled recovery of edits made by a CRISPR base editor in live cells (Fig. 4). Finally, the system is versatile, operating not only in cell culture but also in chick embryos and adult mouse brain tissue (Fig. 5) and is therefore suitable for in vivo barcoding applications (Fig. 6). Taken together, these results indicate that this simple protocol allows high-density barcoding and recording with in situ readout.

Concatenating multiple 20-bp barcodes, as in Fig. 6, can enable combinatorial libraries of distinct barcodes. We tested a modest library of 81 barcodes here. However, the same design could be scaled up to produce an exponential increase in coding capacity. For example, an array of 12 barcode positions, with three barcode variants per position, could achieve a potential barcode diversity of 531,441 variants, similar to that used in sequencing-based barcoding applications[49–51], while requiring only 240 bp of sequence and nine rounds of imaging for readout (an error-correcting coding scheme would require additional hybridization rounds). Coding capacity could be further expanded by inserting multiple arrays at distinct, spatially resolvable genomic sites[16].

Zombie should thus enable viral barcoding with imaging readout. In viral barcoding, cells are labeled at a single time-point or, more recently, at multiple time-points[51], to enable subsequent identification of their descendants[10]. Viral barcoding methods have revolutionized the study of hematopoietic development[49,52], neurobiology[53,54] and cancer[55]. They have also enabled new high-throughput screening approaches[56]. However, so far, researchers have predominantly relied on sequencing for readout of virally delivered barcodes. Diverse combinatorial libraries of short Zombie-readable barcodes should enable simultaneous recovery of lineage, cell fate and spatial organization in diverse settings, including development, regeneration and cancer. Similarly, Zombie can facilitate multiplexed high-throughput screening, in which cellular phenotypes are assayed by imaging and connected to genetic or environmental perturbations that are identified by barcodes[57].

An immediate application of Zombie will be to enable improved recording systems with image-based readout. In the previously described MEMOIR recording system, Cas9 stochastically and continuously edited ~1-kb barcoded memory elements over multiple cell cycles[2]. These edits resulted in large-scale sequence deletions, providing only a single binary memory state per kilobase of sequence. By contrast, in situ readout of base edits could provide a much higher memory density[8,9]. Additionally, by circumventing the need for barcode expression in living cells, this approach avoids issues with burstiness in expression and stochastic silencing. This approach should thus enable a more powerful imaging-based recording system, while maintaining compatibility with subsequent transcriptome readout, for example, by seqFISH[15,58], in the same cells.

There has appeared to be a general trade off between sequencing-based approaches that provide high-throughput single-nucleotide level readout but no spatial context and imaging approaches that preserve spatial information but lack the sensitivity of sequencing. Recent work has begun to bridge this gap in both directions[46,59–61]. By allowing imaging-based detection with sensitivity and scalability comparable to sequencing, we anticipate that Zombie will facilitate imaging-based barcoding, recording and other applications, which are currently dominated by sequencing.

Material availability

Plasmids and cell lines described in this paper are available, upon request, from the corresponding author.

Reporting Summary. Further information on research design is available in the Nature Research Reporting Summary linked to this article.

Online content

Any methods, additional references, Nature Research reporting summaries, source data, extended data, supplementary information, acknowledgements, peer review information; details of author contributions and competing interests; and statements of data and code availability are available at https://doi.org/10.1038/s41587-019-0299-4.

References

1. Farzadfard, F. & Lu, T. K. Emerging applications for DNA writers and molecular recorders. *Science* **361**, 870–875 (2018).
2. Frieda, K. L. et al. Synthetic recording and in situ readout of lineage information in single cells. *Nature* **541**, 107–111 (2017).
3. McKenna, A. et al. Whole-organism lineage tracing by combinatorial and cumulative genome editing. *Science* **353**, aaf7907 (2016).
4. Alemany, A., Florescu, M., Baron, C. S., Peterson-Maduro, J. & van Oudenaarden, A. Whole-organism clone tracing using single-cell sequencing. *Nature* **556**, 108–112 (2018).
5. Kalhor, R et al. Developmental barcoding of whole mouse via homing CRISPR. *Science* **361**, eaat9804 (2018).
6. Raj, B. et al. Simultaneous single-cell profiling of lineages and cell types in the vertebrate brain. *Nat. Biotechnol.* **36**, 442–450 (2018).
7. Spanjaard, B. et al. Simultaneous lineage tracing and cell-type identification using CRISPR–Cas9-induced genetic scars. *Nat. Biotechnol.* **36**, 469–473 (2018).
8. Farzadfard, F et al. Single-nucleotide-resolution computing and memory in living cells. *Mol. Cell* **75**, 769–780 (2019).
9. Tang, W. & Liu, D. R. Rewritable multi-event analog recording in bacterial and mammalian cells. *Science* **360**, eaap8992 (2018).
10. Kebschull, J. M. & Zador, A. M. Cellular barcoding: lineage tracing, screening and beyond. *Nat. Methods* **15**, 871–879 (2018).
11. Kalhor, R., Mali, P. & Church, G. M. Rapidly evolving homing CRISPR barcodes. *Nat. Methods* **14**, 195–200 (2017).
12. Livet, J. et al. Transgenic strategies for combinatorial expression of fluorescent proteins in the nervous system. *Nature* **450**, 56–62 (2007).
13. Pei, W. et al. Polylox barcoding reveals haematopoietic stem cell fates realized in vivo. *Nature* **548**, 456–460 (2017).
14. Zheng, G. X. Y. et al. Massively parallel digital transcriptional profiling of single cells. *Nat. Commun.* **8**, 14049 (2017).
15. Shah, S., Lubeck, E., Zhou, W. & Cai, L. seqFISH accurately detects transcripts in single cells and reveals robust spatial organization in the hippocampus. *Neuron* **94**, 752–758 (2017).
16. Shah, S. et al. Dynamics and spatial genomics of the nascent transcriptome by intron seqFISH. *Cell* **174**, 363–376 (2018).
17. Chen, K. H., Boettiger, A. N., Moffitt, J. R., Wang, S. & Zhuang, X. RNA imaging. Spatially resolved, highly multiplexed RNA profiling in single cells. *Science* **348**, aaa6090 (2015).
18. Wang, X. et al. Three-dimensional intact-tissue sequencing of single-cell transcriptional states. *Science* **361**, eaat5691 (2018).
19. Raj, A., van den Bogaard, P., Rifkin, S. A., van Oudenaarden, A. & Tyagi, S. Imaging individual mRNA molecules using multiple singly labeled probes. *Nat. Methods* **5**, 877–879 (2008).
20. Choi, H. M. T. et al. Programmable in situ amplification for multiplexed imaging of mRNA expression. *Nat. Biotechnol.* **28**, 1208–1212 (2010).

21. Choi, H. M. T. et al. Third-generation hybridization chain reaction: multiplexed, quantitative, sensitive, versatile, robust. *Development* **145**, dev165753 (2018).

22. Rouhanifard, S. H. et al. ClampFISH detects individual nucleic acid molecules using click chemistry-based amplification. *Nat. Biotechnol.* **37**, 84–89 (2018).

23. Marras, S. A. E., Bushkin, Y. & Tyagi, S. High-fidelity amplified FISH for the detection and allelic discrimination of single mRNA molecules. *Proc. Natl Acad. Sci. USA* **116**, 13921–13926 (2019).

24. Mitra, R. D. et al. Fluorescent in situ sequencing on polymerase colonies. *Anal. Biochem.* **320**, 55–65 (2003).

25. Ke, R. et al. In situ sequencing for RNA analysis in preserved tissue and cells. *Nat. Methods* **10**, 857–860 (2013).

26. Lee, J. H. et al. Highly multiplexed subcellular RNA sequencing in situ. *Science* **343**, 1360–1363 (2014).

27. Chen, X., Sun, Y.-C., Church, G. M., Lee, J. H. & Zador, A. M. Efficient in situ barcode sequencing using padlock probe-based BaristaSeq. *Nucleic Acids Res.* **46**, e22 (2018).

28. Feldman, D. et al. Optical pooled screens in human cells. *Cell* **179**, 787–799 (2019).

29. Shah, S. et al. Single-molecule RNA detection at depth by hybridization chain reaction and tissue hydrogel embedding and clearing. *Development* **143**, 2862–2867 (2016).

30. Sousa, R. & Mukherjee, S. T7 RNA polymerase. *Prog. Nucleic Acid Res. Mol. Biol.* **73**, 1–41 (2003).

31. Choi, H. M. T. et al. Mapping a multiplexed zoo of mRNA expression. *Development* **143**, 3632–3637 (2016).

32. Vieregg, J. R., Nelson, H. M., Stoltz, B. M. & Pierce, N. A. Selective nucleic acid capture with shielded covalent probes. *J. Am. Chem. Soc.* **135**, 9691–9699 (2013).

33. Levesque, M. J., Ginart, P., Wei, Y. & Raj, A. Visualizing SNVs to quantify allele-specific expression in single cells. *Nat. Methods* **10**, 865–867 (2013).

34. Sternberg, J. B. & Pierce, N. A. Exquisite sequence selectivity with small conditional RNAs. *Nano Lett.* **14**, 4568–4572 (2014).

35. Wu, L. R. et al. Continuously tunable nucleic acid hybridization probes. *Nat. Methods* **12**, 1191–1196 (2015).

36. Symmons, O. et al. Allele-specific RNA imaging shows that allelic imbalances can arise in tissues through transcriptional bursting. *PLoS Genet.* **15**, e1007874 (2019).

37. Mathews, D. H., Sabina, J., Zuker, M. & Turner, D. H. Expanded sequence dependence of thermodynamic parameters improves prediction of RNA secondary structure. *J. Mol. Biol.* **288**, 911–940 (1999).

38. Komor, A. C., Kim, Y. B., Packer, M. S., Zuris, J. A. & Liu, D. R. Programmable editing of a target base in genomic DNA without double-stranded DNA cleavage. *Nature* **533**, 420–424 (2016).

39. Komor, A. C. et al. Improved base excision repair inhibition and bacteriophage Mu Gam protein yields C:G-to-T: Abase editors with higher efficiency and product purity. *Sci. Adv.* **3**, eaao4774 (2017).

40. Gaudelli, N. M. et al. Programmable base editing of A•T to G•C in genomic DNA without DNA cleavage. *Nature* **551**, 464–471 (2017).

41. Li, X. et al. Base editing with a Cpf1–cytidine deaminase fusion. *Nat. Biotechnol.* **36**, 324–327 (2018).

42. Gehrke, J. M. et al. An APOBEC3A–Cas9 base editor with minimized bystander and off-target activities. *Nat. Biotechnol.* **36**, 977–982 (2018).

43. Chan, M. et al. Molecular recording of mammalian embryogenesis. *Nature* **570**, 77 (2019).

44. Hamburger, V. & Hamilton, H. L. A series of normal stages in the development of the chick embryo. *J. Morphol.* **88**, 49–92 (1951).

45. Lois, C. & Alvarez-Buylla, A. Long-distance neuronal migration in the adult mammalian brain. *Science* **264**, 1145–1148 (1994).

46. Emanuel, G., Moffitt, J. R. & Zhuang, X. High-throughput, image-based screening of pooled genetic-variant libraries. *Nat. Methods* **14**, 1159–1162 (2017).

47. Faedo, A. et al. Developmental expression of the T-box transcription factor T-bet/Tbx21 during mouse embryogenesis. *Mech. Dev.* **116**, 157–160 (2002).

48. Baker, H., Kawano, T., Margolis, F. L. & Joh, T. H. Transneuronal regulation of tyrosine hydroxylase expression in olfactory bulb of mouse and rat. *J. Neurosci.* **3**, 69–78 (1983).

49. Lu, R., Neff, N. F., Quake, S. R. & Weissman, I. L. Tracking single hematopoietic stem cells in vivo using high-throughput sequencing in conjunction with viral genetic barcoding. *Nat. Biotechnol.* **29**, 928–933 (2011).

50. Naik, S. H. et al. Diverse and heritable lineage imprinting of early haematopoietic progenitors. *Nature* **496**, 229–232 (2013).

51. Biddy, B et al. Single-cell mapping of lineage and identity in direct reprogramming. *Nature* **564**, 219–224 (2018).

52. Weinreb, C., Rodriguez-Fraticelli, A. E., Camargo, F. D. & Klein, A. M. Lineage tracing on transcriptional landscapes links state to fate during differentiation. Preprint at https://www.biorxiv.org/content/10.1101/467886v2 (2018).

53. Walsh, C. & Cepko, C. L. Widespread dispersion of neuronal clones across functional regions of the cerebral cortex. *Science* **255**, 434–440 (1992).

54. Kebschull, J. M. et al. High-throughput mapping of single-neuron projections by sequencing of barcoded RNA. *Neuron* **91**, 975–987 (2016).

55. Bhang, H.-E. C. et al. Studying clonal dynamics in response to cancer therapy using high-complexity barcoding. *Nat. Med.* **21**, 440–448 (2015).

56. Dixit, A. et al. Perturb-Seq: dissecting molecular circuits with scalable single-cell RNA profiling of pooled genetic screens. *Cell* **167**, 1853–1866 (2016).

57. Boutros, M., Heigwer, F. & Laufer, C. Microscopy-based high-content screening. *Cell* **163**, 1314–1325 (2015).

58. Eng, C.-H. L. et al. Transcriptome-scale super-resolved imaging in tissues by RNA seqFISH. *Nature* **568**, 235–239 (2019).

59. Satija, R., Farrell, J. A., Gennert, D., Schier, A. F. & Regev, A. Spatial reconstruction of single-cell gene expression data. *Nat. Biotechnol.* **33**, 495–502 (2015).

60. Chen, R. et al. A barcoding strategy enabling higher-throughput library screening by microscopy. *ACS Synth. Biol.* **4**, 1205–1216 (2015).

61. Weinstein, J. A., Regev, A. & Zhang, F. DNA microscopy: Optics-free spatio-genetic imaging by a stand-alone chemical reaction. *Cell* **178**, 229–241 (2019).

Methods

Cell culture. E14 mES cells (ATCC cat. no. CRL-1821) were cultured in medium containing GMEM (Sigma), 15% ES cell FBS qualified (Atlanta Biologicals), 1× MEM non-essential amino acids (Thermo Fisher Scientific), 1 mM sodium pyruvate (Thermo Fisher Scientific), 100 μM β-mercaptoethanol (Thermo Fisher Scientific), 1× penicillin–streptomycin–L-glutamine (Thermo Fisher Scientific) and 1,000 U ml^{-1} leukaemia inhibitory factor (Millipore). Cells were maintained on polystyrene (Falcon) plates coated with 0.1% gelatin (Sigma) at 37 °C and 5% CO$_2$.

HEK293T cells were cultured in 1× DMEM (Corning), 10% FBS (Corning), 1× penicillin–streptomycin–L-glutamine (Corning), 1 mM sodium pyruvate (Corning) and 1× MEM non-essential amino acids (Corning) on polystyrene (Falcon) plates at 37 °C and 5% CO$_2$.

For transient transfections, HEK293T cells were plated in 48-well plates at a density of 125,000 cells per well. The next day, cells were transfected with 1.5 μl of Lipofectamine 2000 (Thermo Fisher Scientific) according to the manufacturer's instruction. Three hundred and fifty nanograms of ABE7.10 plasmid, 150 ng of gRNA expression plasmid and 100 ng of GFP plasmid was used per well. In control wells, ABE7.10 and gRNA plasmids were replaced by pUC19 plasmid (NEB) to maintain the total amount of plasmids transfected at a constant level. Cells were then passaged to 24-well plates the day after transfection.

For in situ detection of barcodes, cells were plated on glass-bottom 96-well plates (Cellvis) that were coated with 20 μg ml^{-1} laminin-511 (Biolamina) for at least 3 h at 37 °C.

Cell line engineering. Sequences of all new constructs, barcodes and probes used in this study are reported in Supplementary Table 1. To create stable polyclonal cell lines, mES cells were cultured in 24-well plates to approximately 70% confluency and co-transfected with 600 ng of donor plasmid (Z1, control or Z3) and 200 ng of modified pX330 plasmid[62] (Addgene, 42230) expressing Cas9 and a gRNA targeting the ROSA26 locus (CAGGACAACGCCCACACACC). Transfection was performed using Lipofectamine LTX with Plus reagent (Thermo Fisher Scientific) according to the manufacturer's protocol. The cells were then passaged to a six-well plate the next day and selected with 500 μg ml^{-1} Geneticin starting at 2 d after transfection.

To establish Z1 and Z3 monoclonal cultures, approximately 1,000 cells from the polyclonal population were cultured on a 10-cm plate, from which individual colonies were picked and expanded. Clones were then genotyped by PCR to ensure that the transgene is inserted properly in one of the ROSA26 loci, the other ROSA26 locus is intact and there is no other integration of the transgene or Cas9 elsewhere in the genome.

Zombie procedure for cell culture samples. Cells were washed with 1× PBS before fixation with a 3:1 (vol:vol) mix of methanol and acetic acid (MAA) at room temperature for 20 min. Cross-linking fixation interferes with transcription by phage RNA polymerases, and therefore, should be avoided before the transcription step. Cells were then washed briefly first with 1× PBS and then with nuclease-free water and subsequently were incubated with the transcription mix (MEGAscript Transcription Kit; Invitrogen) at 37 °C for 3 h. All three RNA polymerases used in this study (T3, T7 and SP6) work at comparable levels. The choice of one polymerase over another in different experiments was mostly arbitrary. After transcription, cells were fixed with 4% formaldehyde solution in PBS for 20 min at room temperature followed by two washes with 5× saline-sodium citrate (SSC) buffer, for 5 min each, to remove traces of formaldehyde.

The samples were then preincubated in hybridization buffer at 37 °C for at least 10 min before overnight incubation at 37 °C in hybridization buffer containing each probe at a concentration of 4 nM. When the experiment involved probe competition or split initiator probes with a 25-bp annealing region, 30% probe hybridization buffer (Molecular Technologies) was used for hybridization and the next day, samples were washed four times (15 min each) at 37 °C with 30% probe wash buffer (Molecular Technologies) to remove excess probes, as previously described[21]. For probes with a 20-bp annealing region, in the absence of competition, 10% hybridization buffer (composed of 10% formamide, 10% dextran sulfate and 2× SSC in RNase-free water) was used for overnight hybridization as previously described[29]. These samples were then washed with a wash buffer composed of 30% formamide, 2× SSC and 0.1% Triton X-100 at room temperature for 30 min, to remove excess probes, followed by a brief wash with 5× SSC.

HCR amplification was performed according to the manufacturer's instruction. In brief, samples were first washed with 5× SSCT (5× SSC with 0.1% Tween 20) for 5 min at room temperature and then incubated with amplification buffer (Molecular Technologies) for at least 10 min at room temperature. Meanwhile, each fluorescently labeled hairpin was prepared by snap cooling (heating at 95 °C for 90 s and cooling to room temperature in a dark drawer for 30 min) in hairpin storage buffer. All the required hairpins were then added to the amplification buffer at the final concentration of 60 μM each. Cells were then incubated in the dark with amplification buffer containing the hairpins for 45 min at room temperature. Subsequently, excess hairpins were removed by five washes with 5× SSCT over 1 h. DAPI was added to the third wash to label nuclei. Nuclei could also be visualized using native fluorescent of H2B–CFP, when it was expressed in the cells (for example, Fig. 1c,d). However, native fluorescence of cytoplasmically expressed

fluorescent proteins could not be detected after the Zombie procedure. Samples were then kept in the dark at 4 °C until imaging.

When additional rounds of hybridization and imaging were required, samples were incubated first with 1× DNase I buffer (Roche, 4716728001) in nuclease-free water at room temperature for 5 min and then with DNase I solution (2 U μl^{-1} of the enzyme in 1× buffer) at 37 °C for 3 h, to digest probes and HCR hairpins from the previous round. Subsequently, samples were washed three times with prewarmed 30% wash buffer at 37 °C (first two washes for 5 min each and the third wash for 15 min). Another round of hybridization and HCR was then performed as described above.

The procedure described above is the main protocol we used in the cell culture experiments reported in this paper. See Supplementary Table 2 and Supplementary Figs. 16–18 for details regarding the variations to this main protocol.

Design of the synthetic memory arrays. Each unit of the memory arrays includes a 20-bp probe site that partially overlaps with a 20-bp gRNA target site. gRNA target sites are followed by a PAM sequence (NGG). To limit the possible outcome of base editing by ABE, gRNAs were designed so that from their position 2 to 10 there is only one 'A' nucleotide, which occurs at position 5. We used Azimuth 2.0 software[63,64] to choose gRNA candidates with high on-target and low off-target scores. Each probe sequence is designed so that its GC content is 50% and its predicted T_m, calculated using the nearest-neighbor method[65], is between 56 and 60 °C. Sequences that form hairpins or dimers and homopolymeric tracts of 5 bp or longer were avoided in the probes. We also avoided recognition sites of certain restriction enzymes (BsaI, BsmBI, BpiI, AarI and XbaI) within the memory arrays to facilitate cloning. For the design 1 array, probe sequences were chosen to differ from each other in at least seven positions, to ensure specificity. For design 2, as all memory units are targeted with the same gRNA, 12 of 20 bp are shared among all probes. We chose the remaining 8 bp so that all probes are different from each other in at least two positions of the first four nucleotides and at least another two positions among the second four nucleotides. Furthermore, to facilitate discrimination, we always mixed probes targeting all 12 design 2 barcodes together, at an equimolar ratio, with the ones not being analyzed in any given experiment at an orthogonal channel (for example, B5 HCR initiator). See Supplementary Table 1 for full sequences of the arrays and their corresponding probes.

Combinatorial barcode library. Synthetic gene fragments containing 81 barcode combinations were obtained from Twist Bioscience and cloned into a lentiviral transfer plasmid by golden gate cloning, using Esp3I and T7 DNA ligase (see Supplementary Table 1 for the sequence of plasmids and barcodes). After transformation into NEB 10-beta chemical competent *E. coli* (C3019I), more than 10,000 colonies were scraped off the plates and used to prepare DNA for lentiviral packaging.

Lentiviral delivery of barcodes. Lentiviral vectors were produced and stored as previously described[66] using the plasmids described above. The viral titer was determined by serial dilution. We only used viral preparations with at least 10^7 infectious units per microliter. To establish stable cell lines, HEK293T cells were resuspended in the culture medium, at a density of 500,000 cells per milliliter. Three microliters of lentiviral preparation was mixed in with 97 μl of cell suspension. Ten microliters of this mix was then added to another 90 μl of cell suspension in a separate tube. After mixing, the cells of the second tube were cultured in a 96-well plate for 3 d, without change of medium. Subsequently, the cells were expanded in fresh medium and used for the experiments.

To deliver barcodes to chicken embryos, fertilized eggs of white leghorn chickens were obtained from McIntyre Poultry and Fertile Eggs and incubated in a humidified atmosphere at 38 °C for 35–40 h. The lentiviral preparation was then injected in the neural tube of embryos ranging between stages HH10 and HH11[44]. After injection, the eggs were closed with Parafilm and kept at 38 °C. The embryos were analyzed 3 d after injection, at day five of incubation (stage HH27).

In mice, lentiviral injections were carried out stereotactically into the olfactory bulb of 3-month-old male BL6 mice (JAX). Mice were anesthetized by a single intraperitoneal injection with a ketamine–xylazine solution. The stereotaxic coordinates were 5.5 mm anterior from bregma, 1.2 mm lateral from the midline and 0.40 mm ventral from the brain surface. We performed a single injection per olfactory bulb using 0.3 μl of the lentiviral preparation. The mouse brains were analyzed either 3 or 12 d after injection, as described in the text.

Note that different viral integration sites or chromatin states could potentially vary in their accessibility to phage polymerases. All the experimental procedures performed on animal models was approved by the Institutional Animal Care and Use Committee of California Institute of Technology.

Next-generation sequencing. gDNA was extracted from cells using DNeasy blood and tissue kit (Qiagen) according to manufacturer instructions. Amplicon libraries containing the regions of interest (that is, memory arrays or library barcodes) were then generated from gDNA with a two-step PCR protocol to add Illumina adapters and Nextera i5 and i7 combinatorial indices. Indexed amplicons were pooled and sequenced on the Illumina MiSeq platform with a 600-cycle, v3 reagent kit (Illumina, MS-102-3003). To analyze next-generation sequencing data, raw

FASTQ files were aligned to a FASTA-format reference file containing the expected amplicon sequences. Alignment was performed using the Burrows–Wheeler alignment tool (bwa-mem)[67]. For the combinatorial viral library (Fig. 6e), the number of reads aligning to each possible reference sequence was computed using a custom script in R, available at https://data.caltech.edu/records/1303. For the base-editing samples (Supplementary Fig. 11), we extracted base calls from each read at the base-editor target sites, as well as the quality scores at these sites. Paired-end reads were merged, accepting the base call with the highest quality score in overlapping regions. Reads with a quality score of more than ten at the target site position were included in the analysis.

Histology. After collection, adult mouse brain and embryonic chicken tissues were washed with cold RNase free 0.1 M PBS, pH 7.4 at 4 °C. Fresh tissues were then immersed into the Tissue-Tek O.C.T. Compound (Electron Microscopy Sciences, 4583) and were frozen immediately for 3 min in isopentane cooled to −70 °C in dry ice. Samples were then stored at −80 °C until sectioning. Twenty-micrometer-thick sections were obtained using a Leica Cryostat, mounted on SuperFrost slides or coverslips coated with 2% vol/vol solution of (3-aminopropyl)triethoxysilane in acetone. Sections were then stored at −80 °C until use.

Zombie procedure for tissue sections. The slides were first left to dry at room temperature for about 5 min and then fixed with MAA at room temperature in a glass staining jar for 3 h. Subsequently, the slides were washed by transfer to a new jar filled with PBS three times for 5 min each. After a brief wash in nuclease-free water, SecureSeal hybridization chambers (Grace Bio-Labs, SKU:621501) were put on the slides and transcription mix (MEGAscript T7 or T3 Transcription Kit; Invitrogen) was added to the sections and incubated for 3 h at 37 °C. After transcription, samples were fixed with 4% formaldehyde in PBS overnight at 4 °C. Formaldehyde was then removed by three washes with 5× SSC at room temperature for 10 min each.

Hybridization was performed similarly to that described above for cell culture samples. Sections were prehybridized with probe hybridization buffer for at least 30 min at 37 °C, before overnight incubation with probe hybridization buffer containing 4 nM of each probe at 37 °C. When the experiment involved probe competition (for example, Fig. 5c–h) or split initiator probes with a 25-bp annealing region (for example, Fig. 5b and Supplementary Fig. 15), 30% probe hybridization buffer (Molecular Technologies) was used for hybridization followed by four 15-min washes at 37 °C with 30% probe wash buffer (Molecular Technologies). For probes with a 20-bp annealing region, in the absence of competition (for example, Fig. 6), 10% hybridization buffer (composed of 10% formamide, 10% dextran sulfate and 2× SSC in RNase-free water) was used for overnight hybridization, followed by two 30-min washes in 30% formamide, 2× SSC and 0.1% Triton X-100 at room temperature. Then, after three brief washes with 5× SSCT at room temperature, sections were incubated with amplification buffer for 20 min, which was then replaced by amplification buffer containing snap-cooled fluorescently labeled hairpins (Molecular Technologies), each at 60 μM. After 1 h of incubation in the dark at room temperature, excess hairpins were removed by five washes with 5× SSCT over 1 h. DAPI was added to the third wash to label nuclei.

For samples that required only one round of hybridization (for example, Fig. 5b–e), hybridization chambers were removed at this point and sections were mounted in Aqua-mount (Thermo Fisher Scientific, 14-390-5) and kept in the dark at 4 °C until imaging. For multiple rounds of hybridization, 5× SSCT was replaced with antibleaching buffer[16] (50 mM Tris-HCl, pH 8.0, 300 mM NaCl, 2× SSC, 3 mM Trolox (Sigma, 238813), 0.8% D-glucose (Sigma, G7528), 100-fold diluted catalase (Sigma, C3155), 0.5 mg ml⁻¹ glucose oxidase (Sigma, G2133) and 0.02 U ml⁻¹ SUPERase in RNase Inhibitor (Invitrogen, AM2694)) and samples were imaged as described below. After imaging, antibleaching buffer was washed first with 5× SSCT and then with 1× DNase I buffer (Roche, 4716728001) in nuclease-free water. Probes and HCR hairpins were then digested by 3 h of incubation with DNase I solution (2 U μl⁻¹ of the enzyme in 1× buffer) at 37 °C for 3 h. Subsequently, the samples were washed three times with prewarmed 30% wash buffer at 37 °C (first two washes for 5 min each and the third wash for 15 min). Another round of hybridization and HCR was then performed as described above.

Imaging. Cell culture samples were imaged on a Nikon Eclipse Ti inverted fluorescence microscope with a Zyla 4.2 sCMOS camera (Andor). We used a ×60 oil objective (1.4 numerical aperture (NA)) and acquired 20 z stacks with 0.5 μm of spacing between them for each position. Positions were chosen solely on the basis of the DAPI channel to avoid bias. Imaging settings, including the exposure times, were kept the same for all the experiments involving cultured cells. Tissue sections were imaged either using ZEN 2.3 (blue edition) on a Zeiss LSM800 confocal microscope with a ×40 (Zeiss 1.2 NA) water-immersion objective (Fig. 5b–e) or using MetaMorph on a Nikon Eclipse Ti inverted microscope equipped with a Yokogawa CSU-W spinning disc unit (Andor), an electron-multiplying charge-coupled device camera (Andor iXon Ultra) and a ×40 (Nikon 1.3 NA) oil objective (Fig. 6 and Supplementary Fig. 15) or a ×60 (Nikon 1.4 NA) oil objective (Fig. 5f–h). The same imaging setting was used for related samples to facilitate comparison between images.

Image analysis. Images were processed and analyzed using MATLAB and Fiji[68], mainly by custom scripts that are available at https://data.caltech.edu/records/1303. For cell culture experiments, maximum-intensity projections of the raw images were used in all analyses.

Segmentation. Segmentation of nuclei and dots was done automatically in MATLAB by filtering and thresholding of the images. However, the results were manually inspected to ensure accuracy. Segmentation of nuclei was done on the basis of either CFP (Figs. 1–3 and 5, and Supplementary Figs. 2, 3, 5, 7, and 12) or DAPI (Figs. 4 and 6, and Supplementary Figs. 8–11) channel. When relevant to the analysis (for example, for efficiency calculations) incorrectly segmented nuclei were manually identified and removed from the analysis. Active site dots were considered to belong to a cell if their center overlapped with the nuclear segmentation of that cell.

Intensity measurement. An estimate of dot intensity, used for Figs. 4e and 5g,h, and Supplementary Figs. 2, 8–12 and 16–18, was obtained by integration of pixel intensities over each dot's segment. A more precise measure of dot intensity[69] was used for Fig. 3d and Supplementary Fig. 7, which was based on fitting a 2D Gaussian to each dot's filtered pixel intensity values and calculating the volume under the surface of the Gaussian.

Co-localization. Co-localization of dots was identified on the basis of close proximity (less than 4 pixels) of the center of segmented dots in two or more channels.

Classification. For single-nucleotide detection, where four probes compete for the same target site (Fig. 3d and Supplementary Fig. 7), to assign a nucleotide to each dot, the natural log of intensity values for that dot in each channel were normalized linearly between 0 and 1, using the intensity values from all the dots detected in that channel across the experiment. The nucleotide associated with the channel that had the highest normalized intensity was then assigned to the dot. Calling the base edits (Fig. 4 and Supplementary Figs. 8–11) as well as A and G classification in vivo (Fig. 5g,h and Supplementary Fig. 12), was done by clustering natural log of intensity values in two groups using k-means clustering with a cosine distance metric (kmeans function, MATLAB).

Registration. Images of HEK293T cells transduced by the combinatorial viral library were registered initially on the basis of the CFP channel, using the normalized cross-correlation method. A more refined registration was then achieved, using the imregtform function in MATLAB, on the basis of dots corresponding to different variant positions, regardless of their fluorescent channel and using the CFP registration as the initial transformation.

Statistical analysis. All experiments were performed in multiple distinct replicates, as indicated in the text and figure legends. Mutual information calculations in Supplementary Fig. 3 were performed as previously described[70], by analyzing pairwise co-localization of barcodes in 564 cells across three replicates. In brief, normalized mutual information (or uncertainty coefficient), U, between two barcodes, x and y, is defined as $U(x|y) = \frac{H(x) - H(x|y)}{H(x)}$, where H is the entropy calculated by the formula $H = -\sum_i p_i \ln(p_i)$, where p_i is the probability of each state, denoted by i, in this case detection or failure to detect a barcode. All statistics and tests are described fully in the text or figure legend.

Data availability

Data that are not included in the paper are available at https://data.caltech.edu/records/1303 (https://doi.org/10.22002/D1.1303) or from the corresponding author.

Code availability

Scripts for all analyses presented in this paper are available at https://data.caltech.edu/records/1303 (https://doi.org/10.22002/D1.1303) or from the corresponding author.

References

62. Cong, L. et al. Multiplex genome engineering using CRISPR/Cas systems. *Science* **339**, 819–823 (2013).
63. Doench, J. G. et al. Optimized sgRNA design to maximize activity and minimize off-target effects of CRISPR–Cas9. *Nat. Biotechnol.* **34**, 184–191 (2016).
64. Listgarten, J. et al. Prediction of off-target activities for the end-to-end design of CRISPR guide RNAs. *Nat. Biomed. Eng.* **2**, 38–47 (2018).
65. SantaLucia, J. Jr. A unified view of polymer, dumbbell, and oligonucleotide DNA nearest-neighbor thermodynamics. *Proc. Natl Acad. Sci. USA* **95**, 1460–1465 (1998).
66. Lois, C., Hong, E. J., Pease, S., Brown, E. J. & Baltimore, D. Germline transmission and tissue-specific expression of transgenes delivered by lentiviral vectors. *Science* **295**, 868–872 (2002).

67. Li, H. Aligning sequence reads, clone sequences and assembly contigs with BWA-MEM. Preprint at https://arxiv.org/abs/1303.3997 (2013).
68. Schindelin, J. et al. Fiji: an open-source platform for biological-image analysis. *Nat. Methods* **9**, 676–682 (2012).
69. Ding, F. & Elowitz, M. B. Constitutive splicing and economies of scale in gene expression. *Nat. Struct. Mol. Biol.* **26**, 424–432 (2019).
70. Press, W. H. et al. *Numerical Recipes in C: The Art of Scientific Computing* (Cambridge Univ., 1992).

Author contributions

A.A., L.S.-G., L.C., C.L. and M.B.E. designed research. A.A., L.S.-G., J.M.L. and M.W.B. performed experiments. A.A., D.M.C. and M.B.E. analyzed data. A.A. and M.B.E. wrote the manuscript.

Competing interests

Authors have submitted a provisional patent application that is based on the technology described in this manuscript.

Additional information

Supplementary information is available for this paper at https://doi.org/10.1038/s41587-019-0299-4.

Correspondence and requests for materials should be addressed to M.B.E.

Reprints and permissions information is available at www.nature.com/reprints.

Corresponding author(s): Michael B. Elowitz

Last updated by author(s): Sep 20, 2019

Reporting Summary

Nature Research wishes to improve the reproducibility of the work that we publish. This form provides structure for consistency and transparency in reporting. For further information on Nature Research policies, see Authors & Referees and the Editorial Policy Checklist .

Statistics

For all statistical analyses, confirm that the following items are present in the figure legend, table legend, main text, or Methods section.

n/a	Confirmed	
☐	☒	The exact sample size (*n*) for each experimental group/condition, given as a discrete number and unit of measurement
☐	☒	A statement on whether measurements were taken from distinct samples or whether the same sample was measured repeatedly
☐	☒	The statistical test(s) used AND whether they are one- or two-sided *Only common tests should be described solely by name; describe more complex techniques in the Methods section.*
☒	☐	A description of all covariates tested
☒	☐	A description of any assumptions or corrections, such as tests of normality and adjustment for multiple comparisons
☐	☒	A full description of the statistical parameters including central tendency (e.g. means) or other basic estimates (e.g. regression coefficient) AND variation (e.g. standard deviation) or associated estimates of uncertainty (e.g. confidence intervals)
☐	☒	For null hypothesis testing, the test statistic (e.g. *F*, *t*, *r*) with confidence intervals, effect sizes, degrees of freedom and *P* value noted *Give P values as exact values whenever suitable.*
☒	☐	For Bayesian analysis, information on the choice of priors and Markov chain Monte Carlo settings
☒	☐	For hierarchical and complex designs, identification of the appropriate level for tests and full reporting of outcomes
☒	☐	Estimates of effect sizes (e.g. Cohen's *d*, Pearson's *r*), indicating how they were calculated

Our web collection on statistics for biologists contains articles on many of the points above.

Software and code

Policy information about availability of computer code

Data collection	Fluorescence microscopy images of cell culture samples were collected using MetaMorph (version 7.8.7.0). Confocal microscopy images were collected using either ZEN 2.3 (blue edition) or MetaMorph (version 7.8.7.0), as described in the methods.
Data analysis	Data analysis was done using custom MATLAB (R2018b), Fiji (downloaded in 2019), and R (version 3.5.2) scripts. All the scripts as well as raw and processed data used to generate figures and representative images in this paper are available from the corresponding author. Azimuth 2.0 software was used to estimate on-target and off-target scores of gRNA candidates.

For manuscripts utilizing custom algorithms or software that are central to the research but not yet described in published literature, software must be made available to editors/reviewers. We strongly encourage code deposition in a community repository (e.g. GitHub). See the Nature Research guidelines for submitting code & software for further information.

Data

Policy information about availability of data

All manuscripts must include a data availability statement. This statement should provide the following information, where applicable:

- Accession codes, unique identifiers, or web links for publicly available datasets
- A list of figures that have associated raw data
- A description of any restrictions on data availability

Data that are not included in the paper are available, upon request, from the corresponding author.

Field-specific reporting

Please select the one below that is the best fit for your research. If you are not sure, read the appropriate sections before making your selection.

☒ Life sciences   ☐ Behavioural & social sciences   ☐ Ecological, evolutionary & environmental sciences

For a reference copy of the document with all sections, see nature.com/documents/nr-reporting-summary-flat.pdf

Life sciences study design

All studies must disclose on these points even when the disclosure is negative.

Sample size	No statistical methods were used to predetermine sample sizes. Experiments were replicated multiple times, as described in the text and figure legends, and 10 to 15 field of views were imaged in each experiment to ensure sufficient representation of variability in the results.
Data exclusions	In each experiment, we excluded a few images in which strong non-specific fluorescence, in one or more channels, interfered with segmentation or quantification. The exclusion was done prior to analysis, based on criteria independent of the objective of the experiment, to avoid bias in the results.
Replication	All attempts at replication were successful.
Randomization	Randomization is not relevant to this study. Samples were allocated into experimental groups based on the treatments performed on them.
Blinding	Investigators were not blinded to group allocation. However, for all quantitative results, field of views during imaging were chosen solely based on DAPI and/or CFP signal to avoid bias.

Reporting for specific materials, systems and methods

We require information from authors about some types of materials, experimental systems and methods used in many studies. Here, indicate whether each material, system or method listed is relevant to your study. If you are not sure if a list item applies to your research, read the appropriate section before selecting a response.

Materials & experimental systems

n/a	Involved in the study
☒	☐ Antibodies
☐	☒ Eukaryotic cell lines
☒	☐ Palaeontology
☐	☒ Animals and other organisms
☒	☐ Human research participants
☒	☐ Clinical data

Methods

n/a	Involved in the study
☒	☐ ChIP-seq
☒	☐ Flow cytometry
☒	☐ MRI-based neuroimaging

Eukaryotic cell lines

Policy information about cell lines

Cell line source(s)	E14 mouse embryonic stem cells (ATCC) HEK293T cells (ATCC)
Authentication	Cell lines were not authenticated.
Mycoplasma contamination	Cell lines were not tested for mycoplasma contamination.
Commonly misidentified lines (See ICLAC register)	No commonly misidentified cell lines were used in this study.

Animals and other organisms

Policy information about studies involving animals; ARRIVE guidelines recommended for reporting animal research

Laboratory animals	Mice: 3 month old, male C57BL/6J Chicken: embryonic stage HH10 through HH27, white leghorn
Wild animals	No wild animals were used in this study.

| Field-collected samples | No field-collected samples were used in this study. |
| Ethics oversight | All the experimental procedures performed on animals was approved by the Institutional Animal Care and Use Committee of California Institute of Technology. |

Note that full information on the approval of the study protocol must also be provided in the manuscript.